Evolution of permeability in heterogeneous granular aggregates during chemical compaction: Granular mechanics models

Baisheng Zheng[1] and Derek Elsworth[1]

Received 9 June 2011; revised 20 January 2012; accepted 23 January 2012; published 13 March 2012.

[1] We develop a granular mechanics model to represent the process of chemical compaction within granular media. This model represents the serial processes of stress-enhanced dissolution, mass diffusion along the fluid film separating grain boundaries, and then mass ejection into the pore space, where it may then be either reprecipitated onto the pore wall or removed by fluid advection in an open system. This process is controlled by the evolution of intergranular effective stress and mass concentrations in the fluid either in the water film or the pore space. The evolution of intergranular stress is followed by a granular mechanics model that rigorously couples the magnitude of the grain-grain contact stress to determine the time history of stress-driven dissolution. Pore fluid concentration provides a feedback to intergranular dissolution, halting intergranular compaction as fluid concentrations approach aqueous saturation. Importantly, chemical feedbacks onto the mechanical system and mechanical feedbacks on the chemical system are rigorously accommodated. Compaction is halted either by the amelioration of the driving stress (through the growth of the contact area) or by the saturation of the fluid in the pore space. This model is used to explore the influence of heterogeneous assemblages of particles on the rate and ultimate magnitude of compaction and the resulting evolution of permeability. Specifically, we explore the influence of heterogeneity in granular packs by using heterogeneous distributions of particles (linear, Gaussian, or bimodal). Results indicate that porosity and permeability decrease with compaction. Small particles dominate this dissolution-mediated process and accelerate compaction; this is true both for homogeneous distributions of small particles and for coarser aggregates containing a fraction of smaller particles. Overall, compaction is also greater for finer aggregates resulting from the larger deformation required, reaching the critical stress that will halt compaction. This feature is due to the necessary redistribution of intergranular stresses that are shed from point contacts in active chemical dissolution onto those not deforming.

Citation: Zheng, B., and D. Elsworth (2012), Evolution of permeability in heterogeneous granular aggregates during chemical compaction: Granular mechanics models, *J. Geophys. Res.*, *117*, B03206, doi:10.1029/2011JB008573.

1. Introduction

[2] The interaction of mechanical and chemical effects exerts significant influence on the evolution of permeability [*Yasuhara et al.*, 2003] and strength [*Yasuhara et al.*, 2005] of granular aggregates and of fractures [*Yasuhara et al.*, 2004]. These feedbacks may involve reduction in permeability as stress-mediated dissolution removes porosity [*Revil*, 1999; *Yasuhara et al.*, 2003, 2004], augments porosity by wormholing [*Andre et al.*, 2007; *Bemer and Lombard*, 2010; *Polak et al.*, 2004] or occludes porosity by precipitation [*Bekri et al.*, 1995, 1997; *Cussler*, 1982]. Similarly, changes in strength result from interface bonding mediated by dissolution and precipitation [*Niemeijer et al.*, 2010; *Yasuhara et al.*, 2005] and by subcritical crack growth among other mechanisms [*Chester et al.*, 2007]. These processes that evolve at the microscopic scale exert important influences on the macroscopic behavior of granular media and are important in understanding rupture, reactivation and healing on faults and in linking triggered seismicity and permeability evolution in geothermal, sequestration and hydrocarbon reservoirs. This work focuses on the effects of stress-mediated chemical effects in defining the evolution of strength and permeability during chemical compaction.

[3] Chemical compaction results where the elevated contact stresses at grain-grain or asperity-asperity contacts elevates the chemical potential of the mineral allowing the presence of water film to redistribute the dissolving mass. This grain-grain contact may be considered as a thin water

[1]Energy and Mineral Engineering and Energy Institute, Pennsylvania State University, University Park, Pennsylvania, USA.

0148-0227/12/2011JB008573

film [*Revil*, 2001; *Rutter*, 1976] at the contact face or as a dynamic island-channel network [*Lehner*, 1995; *Raj*, 1982; *Schutjens and Spiers*, 1999] supplied by dissolved mineral mass as the activity of the stressed minerals in contact with the fluid is elevated. Dissolution at the stressed contact is thermodynamically favored [*Paterson*, 1973]. The dissolved concentration in the contact area is elevated over that in the pore space allowing diffusion from the high-concentration intergranular area to the low-concentration pore space. Eventually, mineral reprecipitation to the hydrostatically stressed pore walls may occur, depending on the rates of flushing of the pore space with any advective flux. These processes may result in permeability reduction owing to compaction of the granular assemblage and the filling of the pore space and has been successfully applied to explain important phenomena such as diagenetic compaction and fault healing and sealing [*Sleep et al.*, 2000; *Tada and Siever*, 1989; *Yasuhara et al.*, 2005] in crustal rocks.

[4] A variety of models have been applied to represent the mechanics of chemical compaction [*Dewers and Hajash*, 1995; *Gundersen et al.*, 2002; *He et al.*, 2003; *Lehner*, 1995; *Renard et al.*, 1997; *Revil*, 2001; *Yasuhara et al.*, 2003]. *Gundersen et al.* [2002] presented a fully mechanistic model with implicit coupling between dissolution, diffusion, and precipitation. *Yasuhara et al.* [2003] introduced an approach for the implicit coupling of a larger linear equation system which did not require an iterative solution but was able to solve for the compaction of a single grain-grain assemblage and by inference relate this to reservoir diagenesis. Other models have extended this to include feedbacks of pore fluid concentration on the compaction process [*Taron and Elsworth*, 2010] and to allow the arrest of compaction depending on the elevated concentration within the pore fluids. However, the coupling in each of these models is unidirectional and reflects only the effect of the mechanical loading on chemical compaction; there is no reverse feedback from the effects of chemical creep on the mechanical behavior of the granular aggregate. Chemical compaction induced by mechanical loading with the resulting saturation of the pore fluids in the granular system may result in the loss of porosity and permeability and will also affect properties such as density and cohesive and frictional strength of the granular material. In this work we examine the effect of heterogeneous mixtures of particles to determine the influence of grain size distribution on rates of compaction and permeability evolution using a model that accommodates the arrest of compaction by oversaturated fluids [*Taron and Elsworth*, 2010] and therefore accommodates the role of fluid fluxes in the diagenesis of reservoirs and faults. The approach of *Yasuhara et al.* [2003] and *Taron and Elsworth* [2010] is followed and a fully coupled granular mechanics model is developed to accommodate heterogeneous distributions of particles where the evolution of permeability and porosity may be followed during mechanical and chemical compaction.

2. Chemical Model

[5] Mechanically mediated chemical compaction occurs as contact stresses elevate the chemical potential of the solid in the presence of water. This elevated potential favors dissolution into the water film, diffusion along the grain contact and potentially reprecipitation as the mineral mass is ejected into the pore fluid. This behavior may be represented (see Figure 1) by the three processes of (1) dissolution at the stressed interfaces of grain-to-grain contacts, (2) diffusive transport of dissolved matter from the interface to the pore space and, finally, (3) reprecipitation at the wall of the pore space [*Revil*, 2001; *Shimizu*, 1995]. The process is driven by differences in effective normal stress; hence the normal component of solid chemical potential $\Delta\mu$ between grain contacts and free pore walls [*Heidug*, 1995; *Lehner*, 1995; *Paterson*, 1973] is defined as

$$\Delta\mu = \sigma_a V_m + \Delta f - U_s, \tag{1}$$

where V_m is the molar volume, Δf is the molar Helmholtz free energy and U_s is the surface energy term.

[6] With the driving force for pressure solution represented by the chemical potential difference in equation (1) dissolution at the grain-grain contacts will first occur which will provide a source of mass transported by the later processes of diffusion and reprecipitation. The rate of compaction is influenced both by the absolute rate of mass diffusion along this interface and by the lengthening of the diffusion path as the grains interpenetrate and the contact area grows. The strain rate at the grain boundary may be defined as [*Raj*, 1982; *Revil*, 1999]

$$\dot{\varepsilon}_{diss} = \frac{3V_m k_+}{RTd}(-\Delta\mu), \tag{2}$$

where $\dot{\varepsilon}_{diss}$ is the strain rate, k_+ is the dissolution rate constant of quartz, which can be obtained by experimental results, R is the gas constant, T is the temperature of the system and d is the grain diameter. When the disjoining pressure σ_a in equation (1) reaches the critical stress σ_c, the system will reach a state of equilibrium.

[7] For the condition representing uniaxial compression for two particles inline, the disjoining pressure, σ_a, is subject to nonhydrostatic stress. With the assumption that the stress applied at the contact area does not vary with the location of the interface, disjoining pressure, σ_a, can be given by

$$\sigma_a = \frac{\sigma_{eff}}{\varphi}, \tag{3}$$

where σ_{eff} is the effective stress, defined as the average stress acting on the interface between the grains in excess of the pore pressure, and $\varphi(0 < \varphi < 1)$ is the ratio of contact area to the maximum cross-sectional area which is the area of great circle of small particle in each contact normal to the applied stress.

[8] The critical stress σ_c, is defined as [*Revil*, 1999]

$$\sigma_c = \frac{E_m(1 - T/T_m)}{4V_m}, \tag{4}$$

where E_m and Tm are the heat and temperature of fusion, respectively (for quartz, E_m = 8.57 kJ mol^{-1}, T_m = 1883 K). Using the critical stress, the chemical potential difference of equation (1) can be expressed as

$$-\Delta\mu \approx (\sigma_a - \sigma_c)V_m. \tag{5}$$

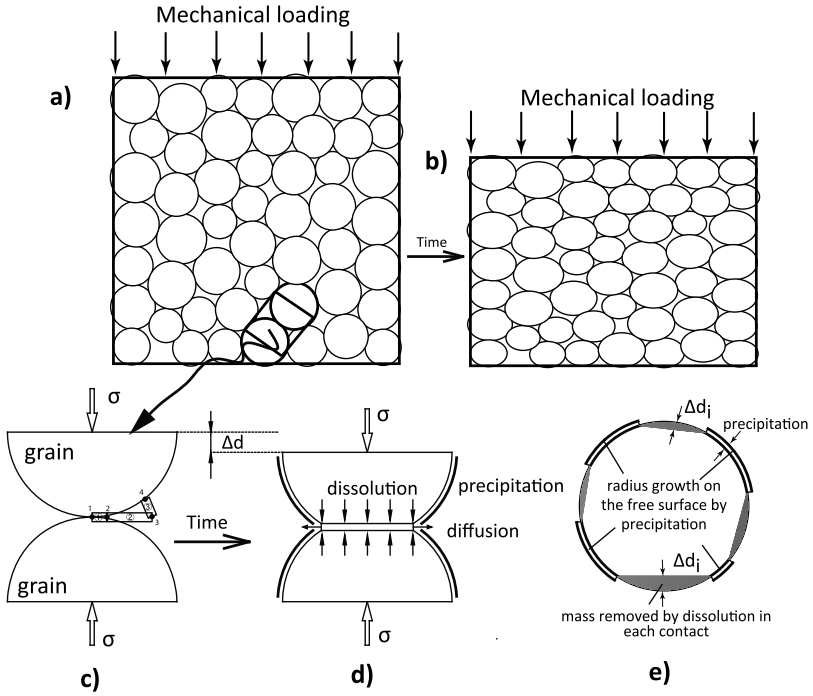

Figure 1. Schematic of pressure solution for (a and b) macroscopic aggregate and microscopic twin contacting grains. At the contacts the mineral dissolves owing to high localized stresses and dissolved mass diffuses from the interface into the pore space. Finally, precipitation occurs at the free faces of the pore walls, resulting in (c and d) the porosity (and related permeability) reduction [see *Yasuhara et al.*, 2003]. (e) The mass precipitated on the free pore wall from the mass removed by dissolution makes each particle radius growth isotropically.

If we substitute the chemical potential into the relation defining dissolution strain (equation (5) into equation (2)), the dissolution rate is given by

$$\dot{\varepsilon}_{diss} = \frac{3V_m^2 k_+}{RTd}(\sigma_a - \sigma_c). \tag{6}$$

The transport of the mineral mass enables the particle surface contraction velocity $\dot{U}^{ch}$ (induced by chemical compaction) to be evaluated from the creep strain as

$$\dot{U}^{ch} = \dot{\varepsilon}_{diss} \times d, \tag{7}$$

where d is the separation between the centers of two contacting spheres and the product of $\dot{U}^{ch} \times \Delta t$ is used to define the incremental deformation of adjacent particles at that contact. Here Δt is the time step for chemical compaction. This information is passed to the mechanical computation in the granular mechanics model as a new increment of deformation due to chemical compaction effects. This is accommodated as the new position of each particle and a new relation in the development of overlap at each contact to enable the updating of contact forces based on Newton's law of motion and the spring constant applied between particles.

[9] The mass redistribution induced by the process of dissolution can be described by the dissolution mass flux, dM_{diss}/dt, which is related to the (grain interpenetration) strain rate. In one dimension the strain rate can be approximated as

$$\dot{\varepsilon}_{diss} \approx \frac{1}{d}\frac{\Delta d}{\Delta t}, \tag{8}$$

where d is grain diameter. By using the dissolution mass flux, dM_{diss}/dt, $\Delta d/\Delta t$ can be expressed as

$$\frac{\Delta d}{\Delta t} \approx \frac{dM_{diss}}{dt}\frac{1}{\rho_g}\frac{1}{(\pi/4)d_c^2}, \tag{9}$$

where ρ_g is the grain density (2560 kg m^{-3} for quartz) and d_c is the diameter of grain-to-grain contact. Substituting equations (6) and (8) into (9), the dissolution mass flux, dM_{diss}/dt, is given by

$$\frac{dM_{diss}}{dt} = \frac{3\pi V_m(\sigma_a - \sigma_c)k_+\rho_g d_c^2}{4RT}. \tag{10}$$

After dissolution has been induced the dissolved mass is transported from high concentration to low concentration along the water film at the interface of the grain-grain contact via diffusion. On the basis of the steady form of Fick's first law the diffusive mass flux dM_{diff}/dt may be evaluated from equation (11) as

$$\frac{dM_{diff}}{dt} = \frac{2\pi\omega D_b}{\ln(d_c/2a)}(C_{\text{int}} - C_{pore}) \tag{11}$$

where D_b is the diffusion coefficient, ω is the thickness of the water film at the interface of the grain-grain contact, $(C_{int})_x = a$ and $(C_{pore})_x = d_c/2$ are concentrations at the center of the interface between grains and at the external contour of that interface, respectively, and a is a small number relative to the grain diameter d_c. This defines the rate of mass diffusion along the evolving interface between grains.

[10] The third mechanism of transport is that of either dissolution or of reprecipitation. The dissolved mass transported along the grain-grain contacts that diffuses from the intergranular contact into the pore space is available to precipitate on the exposed pore wall. Precipitation can be described by the rate of precipitation dM_{pre}/dt

$$\frac{dM_{pre}}{dt} = V_p \frac{A}{M} k_{-}(C_{pore} - C_{eq}^{h}) \tag{12}$$

where A is the relative interfacial area between the solid and aqueous phases and M is the relative mass of water in the system, C_{eq}^{h} is the mass concentration at equilibrium in the hydrostatic state, V_p is the volume of the pore space, and k_{-} is the precipitation rate constant of the mineral, in this case quartz.

[11] An algorithm that accommodates these three serial mechanisms of dissolution, diffusion then reprecipitation is implemented at individual grain-grain contacts in the granular mechanics model. Two hemispheres representing each grain-grain contact are represented as a single element (see Figure 1). At the beginning of the calculation the concentration of the mineral in the interface (this is initially a point contact) and the pore are set to be identical. Once stressed, mass transport by the three serial processes of dissolution, diffusion and reprecipitation are calculated simultaneously by equations (6), (11), and (12) in each time step Δt. This mass transport will induce changes in the concentration at the interface of the grain-grain contact and pore fluid. This concentration is updated at the end of the each time step Δt as [*Yasuhara et al.*, 2003]

$$\begin{Bmatrix} C_{\text{int}} \\ C_{por} \end{Bmatrix}_{t+\Delta t} = \begin{bmatrix} D_1 + V_p/4\Delta t & -D_1 \\ -D_1 & D_1 + D_2 + V_p/2\Delta t \end{bmatrix}^{-1} \cdot \left[\begin{Bmatrix} dM_{diss}/dt \\ D_2 C_{eq}^{h} \end{Bmatrix} + \frac{1}{4\Delta t} \begin{bmatrix} V_p & 0 \\ 0 & 2V_p \end{bmatrix} \begin{Bmatrix} C_{\text{int}} \\ C_{por} \end{Bmatrix}_t \right] \tag{13}$$

where

$$D_1 = \frac{2\pi\omega D_b}{\ln(d_c/2a)},\ D_2 = V_p \frac{A}{M} k_{-}. \tag{14}$$

The cycling of this process is shown in the flowchart of Figure 2.This algorithm defines the evolution of dissolved mass concentrations at the contacts but requires knowledge of mechanical stresses from the contact algorithm for the deformation behavior. In this analysis the effective stress evaluated at the grain contacts is compared against the critical stress to determine if the process will arrest. In addition the aqueous concentration at the interface between each grain-grain contact is compared against the solubility of the aqueous mineral in the state of nonhydrostatic stress C_{eq}^{σ} [see *Taron and Elsworth*, 2010, equation (5)]. Pressure solution creep (described above) is allowed to continue (the PSC model in Figure 2) only if the effective stress is larger than the critical stress and the concentration at the interface is greater than C_{eq}^{σ}. Otherwise the process of dissolution in the interface of the grain-grain contact will cease.

[12] The change in size of each particle is also evaluated as a result of the dissolved mass reprecipitated onto the surface of an individual grain (see Figure 1e). Each target particle i, is surrounded by several pores and contacts. For each contact, a part of the mineral mass transported into the pore within the fluid reprecipitates on the free surface of the pore. For each particle, mass only precipitates on the free surface in contact with the pore. However, for the model the individual particles must remain circular. We solve this dichotomy by allowing the particles to grow isotropically by the amount that would deposit on the open pore surface (excluding the contact) and extend this circular contour over the contact. This fictitious contact is overclosed within the contact and is accommodated. This allows the particle to grow at the correct rate on the pore wall with a fictitious overlap at the contact that is corrected for this excess interpenetration. This is calculated at the end of each chemical cycling time step. For the specific contact between target grain i and pore j which is one of pores around i, the mass reprecipitated onto particle i is evaluated as

$$\Delta M_i = V_p \frac{A}{M} k_{-}(C_{pore} - C_{eq}^{h}) \times \Delta t_{ch} \times \frac{A_i}{A_{ij}} \tag{15}$$

where ΔMi is the mass reprecipitated on particle i, and A_i is the area of the pore wall of particle i and A_{ij} is the total tributary pore wall area present at the contact of particles i and j. Assuming there are n pores around particle i, therefore the total mass M_i^T on the particle is given as

$$M_i^T = \sum_{\eta=1}^{n} \Delta M_{i\eta} \tag{16}$$

and particle i grows by radius Δr in one time step as

$$\Delta r = \frac{M_i^T}{\rho} \frac{1}{\sum A_i} \tag{17}$$

where ρ is the density of the material and ΣAi is the total free surface of target particle i in the pore space.

3. Mechanical Model

[13] The coupling between the mechanical and chemical behaviors is completed through the iterative solution of Newton's second law in a standard fashion within the granular mechanics algorithm (PFC^{2D}). An appropriate constitutive model [*Goodman*, 1980] must include both the nonreactive mechanical behavior supplemented by the behavior induced by chemical compaction. A parallel-bond model is chosen to represent the effect of cementation between contacting particles.

3.1. Parallel-Bond Particle Model

[14] The parallel-bond model relates the constitutive behavior of a finite-sized piece of cementitious material deposited between two particles. The two particles are

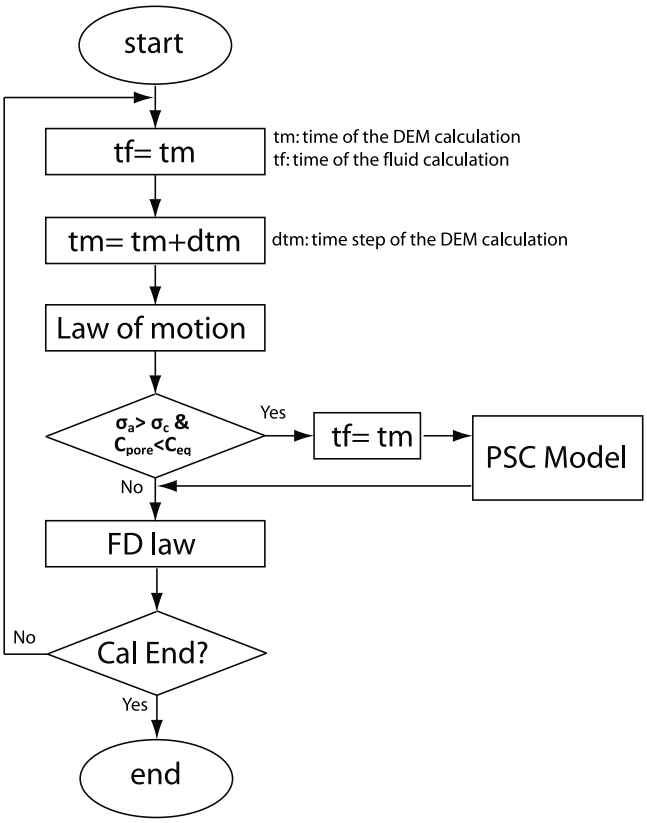

Figure 2. Flowchart of PFC2D showing the algorithm for the chemical scheme. The PSC model is triggered when the critical stress is less than the effective stress and concentration in the interface at the contact is less than the concentration at the stressed point.

envisioned as either spheres or cylinders in the parallel-bond logic. These bonds construct an elastic interaction relationship between particles that works together with slip models. The parallel-bond model simulates the effects of chemical bonding by adding a tension contact with a defined stiffness and resistance to bending on the axis of the particles but allows slip between them. For specific particle i, which has a contact with particle j, the elastic force increments occurring over each mechanical time step of Δt_m are calculated by

$$\Delta \bar{F}^n_{ij} = (-\bar{k}^n A \Delta U_{ij}) n_{ij}$$
$$\Delta \bar{F}^s_{ij} = -\bar{k}^s A \Delta U^s_{ij} \quad (18)$$

where $\bar{k}^n$ and $\bar{k}^s$ are the stiffness in the normal and shear direction of the material, respectively, A is the area of the bond cross section; and $\Delta U_{ij} = V_{ij} \times \Delta t_m$, V_i is the relative velocity of particle i to particle j. This is an efficient way to use the parallel-bond model to represent the mechanical behavior of the granular material after chemical compaction, especially to determine how the stiffness and strength of the material grows after chemical creep.

3.2. Constitutive Model

[15] A new constitutive model is added to accommodate the behaviors induced by chemical compaction. This allows the logic of the granular mechanics algorithm to function with an applied user-defined contact model (UDM) [*Itasca Consulting Group, Inc.*, 2007]. This directly adjusts the contact stiffness and calculates the appropriate contact forces according to relative particle displacements or the contact forces calculated from the last time step. In this manner complex model behaviors may be represented intrinsically within the logic and execution times are significantly faster than if external algorithms are linked to complete this task. The calculation cycle both with and without the UDM is shown in Figure 3. The common feature between them is that both involve a cycle of a law of motion and force displacement law, and the force displacement laws provide contact forces such as those representing normal, shear and frictional resistances. However, the functions of the different force displacement laws are the same. The general structure of a dynamic link library file that constructs a UDM is shown in Figure 4.

[16] In this work, the new constitutive model comprises two parts. The first part represents the mechanical loading with a linear stiffness (shown in Figure 5 as the segment OA) that obeys Hooke's Law with K as the Young's Modulus [*Goodman*, 1980]. The incremental overlap between particles induced by the mechanical loading is set as U_m and the contact force is updated on the basis of equation (18).

[17] The second part represents the chemical compaction process with a constant contact force similar to plastic deformation with no change in stress (as shown by the segment AB in Figure 5). In this part the individual velocity is calculated from equation (19) and the new increment of overlap indicated by U^{ch} is calculated in each chemical time

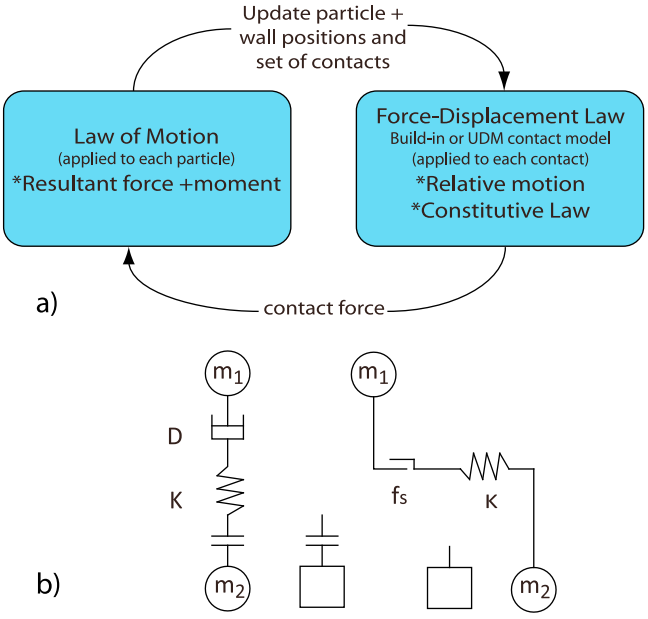

Figure 3. Contact model for the cycling in PFC2D accommodating the constitutive model. New constitutive model shown in Figure 3b is implemented in the part of force displacement law of PFC. The cycling starts from the known particles or walls positions of each contact, and then the force displacement law is applied to update the contact forces. Finally, the law of motion is applied to each particle to update velocity and forces.

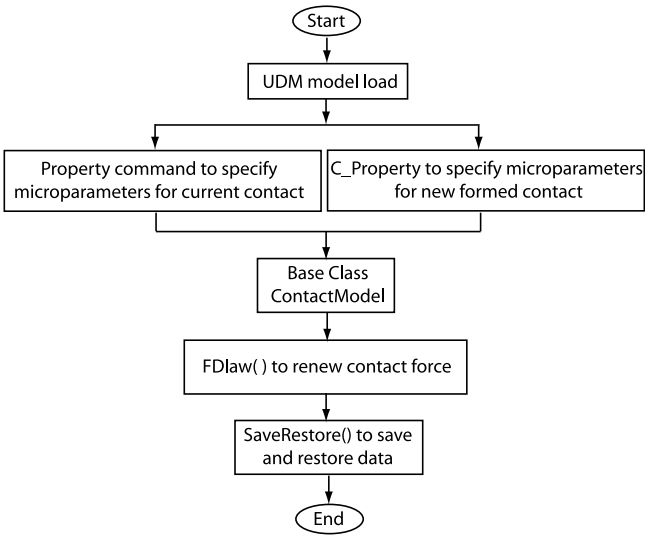

Figure 4. Flowchart for the interaction of both mechanical and chemical influences within the user-defined model (UDM). UDM is implemented in C++, allowing for the changing of properties of each contact and for the addition of new relationships of force and displacement defined by the user.

step Δt. This increment of overlap has no contribution to the contact force as it is used merely to update the new position of the each particle in the Cartesian directions as

$$\begin{aligned} x^i_{t+\Delta t} &= x^i_t + U^{ch}\cdot n_x \\ y^i_{t+\Delta t} &= y^i_t + U^{ch}\cdot n_y \end{aligned} \tag{19}$$

The new position of each particle is used to update the new contact force to be used in Newton's second law of motion to update the other variables of velocity, displacement and force. A dashpot element is used to represent the chemical behavior induced by the process of dissolution. We assume that the contact model contains a spring with constant stiffness K, and a dashpot with variable viscosity D [*Itasca Consulting Group, Inc.*, 2007; *Singh*, 1973a, 1973b; *Stephanson*, 1985] (see Figure 3b).

[18] In the normal direction of this model, the displacement and force law are as follows

$$\begin{aligned} f &= \pm K u_K, f = \pm D\dot{u}_D \\ \dot{f} &= \pm K\dot{u}_K, \dot{f} = \pm D\ddot{u}_D \\ \ddot{f} &= \pm K\ddot{u}_K \end{aligned} \tag{20}$$

where K is the stiffness of the spring, D is the stiffness of dashpot, f is the force acting on spring and dashpot, u_K is the displacement of the spring and u_D is the displacement of dashpot. The resulting displacement and its first derivative relations are

$$\begin{aligned} u &= u_K + u_D \\ \dot{u} &= \dot{u}_K + \dot{u}_D \end{aligned} \tag{21}$$

Substituting equation (20) into equation (21) yields

$$\dot{u} = \pm\frac{\dot{f}}{K} \pm \frac{f}{D} \tag{22}$$

By using a central difference approximation of the finite difference scheme and taking the average value for f,

$$\frac{u^{t+1}-u^t}{\Delta t} = \pm\frac{f^{t+1}-f^t}{K\Delta t} \pm \frac{f^{t+1}+f^t}{2\Delta}. \tag{23}$$

Therefore, the constitutive equation in the form of the central difference approximation is given as

$$f^{t+1} = \pm 1/\left(\frac{1}{K}+\frac{\Delta t}{2D}\right)\left\{u^{t+1} - u^t \mp \left(-\frac{1}{K}+\frac{\Delta t}{2D}\right)f^t\right\}. \tag{24}$$

Here K is a constant based on the contact stiffness between particles and D is a variable based on the behavior at the contact and related to temperature and particle size. The most important attribute of D is that it will change with effective stress and critical stress at each contact with every step. This parameter is derived from the compaction mechanism and is evaluated as

$$D = f/\dot{U}^{ch} \tag{25}$$

The overall cycling within the coupling model first represents mechanical compaction over the short mechanical time Δt^m to calculate the mechanical force balance and then applies chemical compaction to the system on a different time step Δt (see Figure 2) until the chemical strains are equilibrated. As noted previously the contact force and

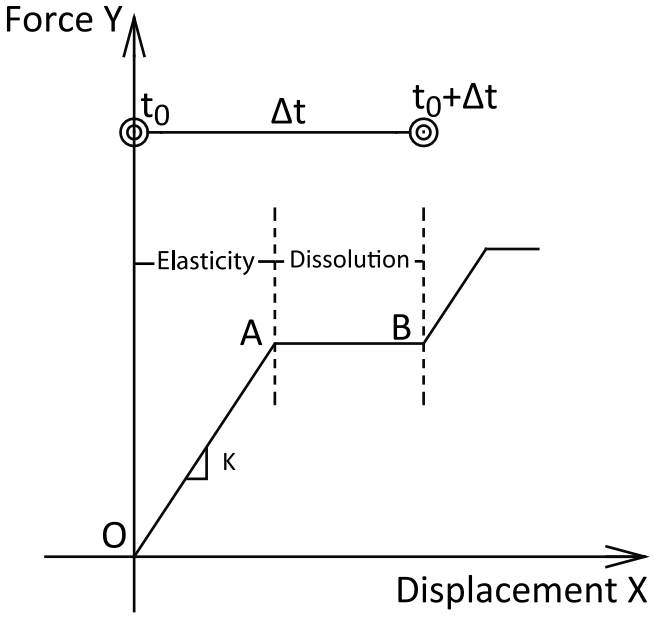

Figure 5. Constitutive model of the deformation force response at particle-particle contacts for both mechanical and chemical interactions. Along segment OA (the contact force is proportional to the overlap following Hooke's law and for the portion involving chemical strains AB) the displacement depends on the chemical gradient, not contact force.

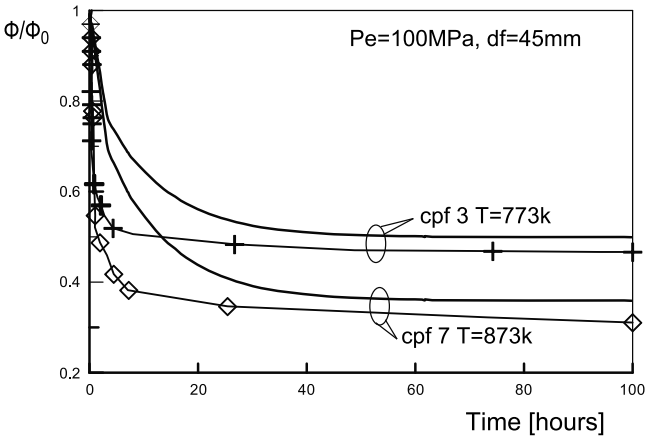

Figure 6. Comparison of the porosity evolution for the model with the chemical compaction experiments of *Niemeijer et al.* [2002]. Lines with symbols are the experimental results. Solid lines are the results from this work with the conditions of applied stress Pe = 100 MPa, and grain diameter df = 45 mm.

velocity is the link between the chemical and mechanical models. The dashpot element is used to match the constitutive requirement induced by the chemical creep behavior. This procedure continues until either the stress at each contact reaches the critical stress or the concentration of the mineral in the fluid in the grain-grain contact and pore space reach an equilibrium concentration. This iterative process is implemented within the user-defined model.

3.3. Permeability

[19] We use this model to explore the evolution of permeability in aggregates where chemical–mechanical effects are coupled. This requires that mechanistically consistent rules are applied to determine permeability from the evolution of porosity and the form of bonding at grain-grain contacts. A capillary model is used to represent the form of the fluid transport path around the deforming and interpenetrating particles [*Bear*, 1972]. In this representation permeability may be related to mean capillary diameter [*Scheidegger*, 1960], δ, as

$$k = \frac{n\delta^2}{96} \tag{26}$$

where n is porosity. Also the relationship between the capillary diameter and the volume of the pore space can be expressed as

$$V_{void} = \frac{\pi}{4}\delta^2 d_0 \tag{27}$$

where we also assume the diameters of capillaries are the same in each domain. Substituting equation (27) into equation (26) and rearranging yields the permeability as

$$k = \frac{nV_{void}}{24\pi d_0} \tag{28}$$

where d_0 is the length between the centers of particles at each contact before deformation and resulting interpenetration. This is the local permeability but the ensemble permeability depends not only on pore characteristics (n and δ), but also on pore connectivity. For each local permeability calculation, the connectivity is related to the void sectional area (A_v) in the direction which is perpendicular to the direction of fluid flow. If $A_v = 0$, then $k = 0$. Otherwise, equation (28) is used to calculated local permeability.

4. Numerical Model and Results

[20] We use this model to explore the evolution of compaction in homogeneous and heterogeneous granular assemblages and to determine the evolution of permeability and porosity in these systems. The model was validated by comparison of the evolution of permeability and porosity with that for twin particles [*Yasuhara et al.*, 2003]. We use granular packs with alternately a Gaussian distribution of initial particle sizes, a linear distribution of particle sizes as noted in Figure 6 and an alternative bimodal model. These granular packs range in the size of the smallest and largest particle sizes to represent either uniform distributions (when the range is low) or heterogeneous distributions (where the range is high).

4.1. Validation

[21] Comparison of the porosity reduction rate (φ/φ_0) of this work with that recovered from experiments [*Niemeijer et al.*, 2002] is shown in Figure 6. Two specific experiments are chosen (*cpf* 3 and *cpf* 7), each conducted at an effective pressure Pe = 100 MPa, and final size of particles df = 45 mm. The model and experimental analyses are in general agreement but with some minor differences. The porosity reduction rate for the numerical model drops more slowly than the experiment, and the final porosity is also smaller than that in the experiment. This may reflect the difference in the experimental and model conditions, where the grain size distribution for the experiment is more uniform that that of the model. Another validation is that shown in Figure 7 which is the comparison of 2D heterogeneous

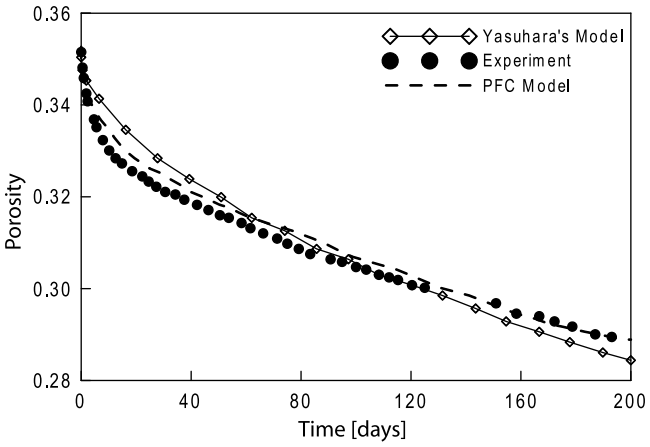

Figure 7. Comparison of porosity evolution during chemical and mechanical compaction with σ_{eff} = 69.9 MPa and T = at 150°C at the open system. The new DEM model is much more accurate; compare with the model of *Yasuhara et al.* [2003] at the early stage of the compaction.

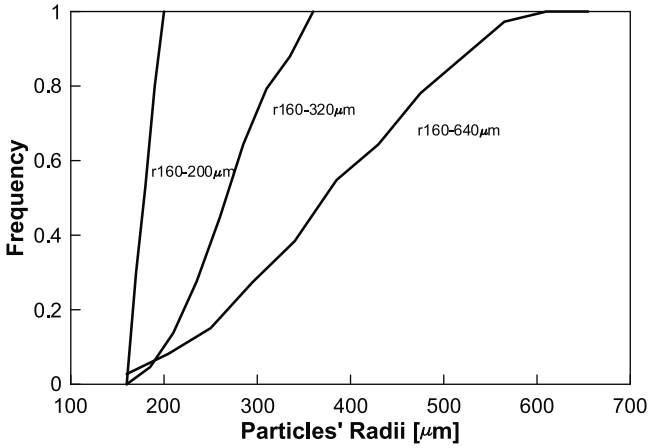

Figure 8. Particle size distribution for homogeneous (model 1, 160–200) and heterogeneous models of different gradations (model 2, 160–320; model 4, 160–640). Frequency distribution conforms to a Gaussian distribution with some particle radii adjusted to fit an initial porosity of 16%.

granular model with experiment and two particles model developed by Yasuhara. It shows that the heterogeneous is much more efficient to represent the porosity loss with chemical compaction. To set the same initial porosity for the model, we must to modify the grain size distribution to meet these starting conditions (see Figure 8). This may reflect the reality that some creep/particle interpenetration has already begun in the experiment, even at the starting conditions. The presence of finer particles in the model may result in the more rapid compaction that is observed in the model relative to the experiment.

[22] Validation has also been completed using the 3-D model which is shown in Figure 9. Compaction experiments have been completed on this aggregate samples of mean grain diameter 180–250 mm at 150°C [*Elias and Hajash*, 1992]. A cross section through the sample shows that before loading

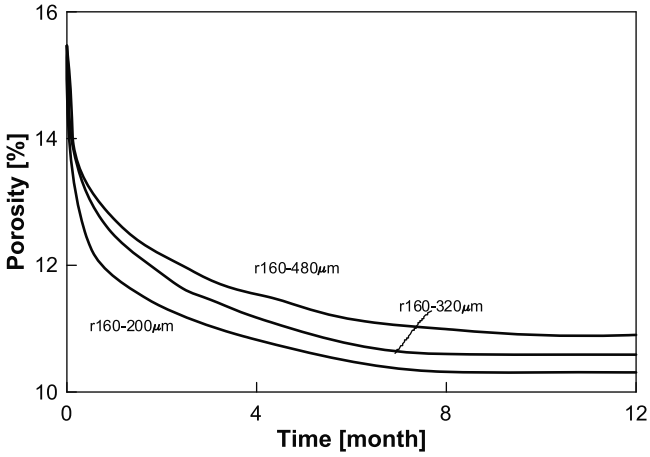

Figure 9. Evolution of the porosity with time for different grain size distributions from homogeneous (model 1, 160–200) to heterogeneous (model 3, 160–480). The models are run under mechanical loads of 20 MPa at a temperature of 300°C.

Table 1. Model With Different Particle Radii Ranges

Particle Size (μm)	Initial Porosity
Uniform Distribution	
180	0.1–0.3
350	0.1–0.3
Gaussian Distribution	
160–350	0.1–0.3
160–200	0.1–0.3
Bimodal Distribution	
100/180	0.1–0.3
100/300	0.1–0.3

the porosity is ~40%. With the application of a mechanical load of 30 MPa, the porosity drops to ~35%. Increasing this mechanical load to an effective stress of σ_{eff} = 69.9 MPa results in a loss in porosity as a result of the triggered chemical and mechanical compaction shown in Figure 10. In the early stages of compaction the new DEM model is much more accurate compared with the result from the model of *Yasuhara et al.* [2003]. In the first 10 days of the experiment the porosity drops quickly and the model is able to better follow the experimental results, compared to the simple two-grain model. In the representation of this behavior the lateral movement of particles makes a significant contribution to the loss of porosity.

4.2. Models

[23] The models listed in Tables 1 and 2 were assembled and executed in the granular mechanics algorithm described previously. Three different distributions were adopted and the corresponding models are of uniform grain diameter, with a particle size of 180 μm and a bimodal model which includes two different particle sizes (180 and 100 μm). The number of the particles in the sample is prescribed by the volume ratio; see Table 2. Finally, a model most closely representing real materials is used in which particle size follows a Gaussian distribution [*Van Bramer*, 2007] with the mean and standard deviation defined as

$$u = (r_{hi} + r_{lo})/2$$
$$\theta = (r_{hi} - r_{lo})/2 \tag{29}$$

where the u is the mean value and θ is the standard deviation. Also, r_{hi} and r_{lo} are the radius of the largest particle and the smallest particle, respectively. Figure 8 shows the particle frequency distribution of this Gaussian assemblage representing a real material with the initial porosity set to the uniform value of 16%.

Table 2. Bimodal Model With Different Particle Radii Ranges

100 μm (%)	180 μm (%)
20	80
30	70
40	60
50	50
60	40
70	30
80	20

Table 3. Loading Applied on the Top Particles of Each Model

	Model				
	A	B	C	D	E
Force (N)	100	200	300	390	500
Stress (MPa)	10	20	30	39	50

4.3. Loading

[24] The evolution of porosity is followed using the previously defined procedure to represent chemical compaction. Figure 9 compares the evolution of porosity under identical loading conditions (see model B in Table 3) for the grain size distributions of uniform (160–200 μm) grain size and those with maximum grain sizes two (320 μm^2) and three (480 μm) times the minimum grain size. The three asymptotes show the same trend, that the porosity reduces with the progress of chemical compaction. The narrowest gradation sample (160–200 μm) also has the smallest grain size diameter with the result that compaction is fastest for this sample. As the grain size of the sample becomes larger the rate of compaction reduces, as observed by others [*Niemeijer et al.*, 2010]. The reduction in porosity is also largest for the smallest grain size. In other words, the small particles will dominate the process of the dissolution-mediated chemical compaction in this granular system. The reason is that the overlap of each contact is a linear function of the contact force. When a particle is small, with the same mechanical load, the overlap will be same, but the contact area of small particles will be smaller than that in contact of large particles, which means the stress on the contact area is larger when in contact with small particles. With the larger stress, the creep rate of chemical compaction is greater.

[25] A numerical test was competed to illustrate that the presence of small particles within granular aggregates dominate compaction rate in chemomechanical compaction. Figure 10a is a uniform model with particles at 180 μm. Figures 10b, 10c, and 10d are three heterogeneous models which includes two different size of particles, the smaller particles are 100 μm and the bigger particles are 180 μm and the number of particles in these three model are controlled by the volume ratio. The results are shown in Figure 11. With the same initial porosity at 15%, and same mechanical loading and environmental conditions, the bimodal distribution shows that increasing the proportion of smaller particles

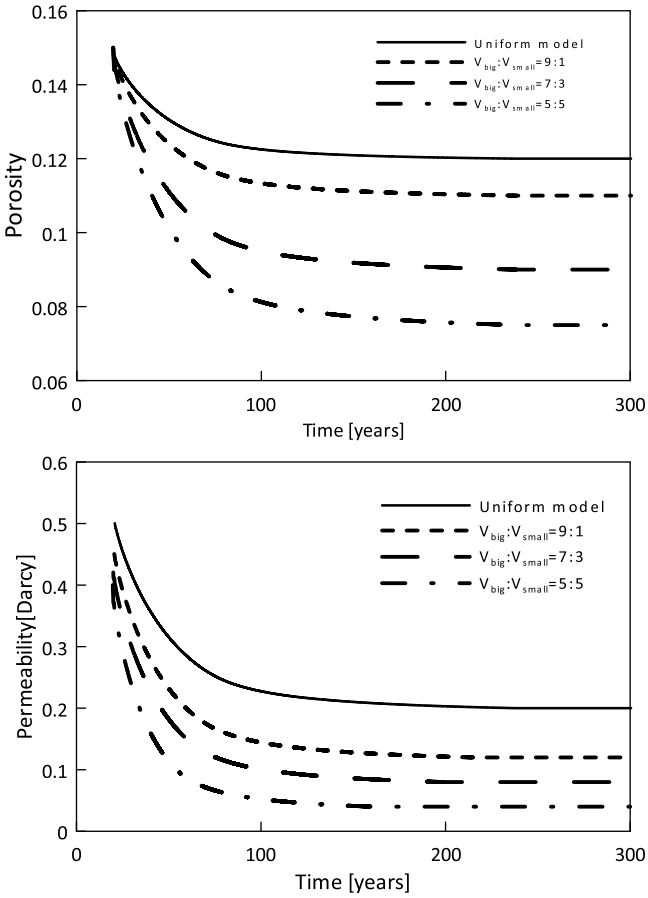

Figure 11. Comparison of (top) porosity and (bottom) permeability evolution during chemomechanical compaction in the uniform model and bimodals which have different volume ratios of big particles to small particles.

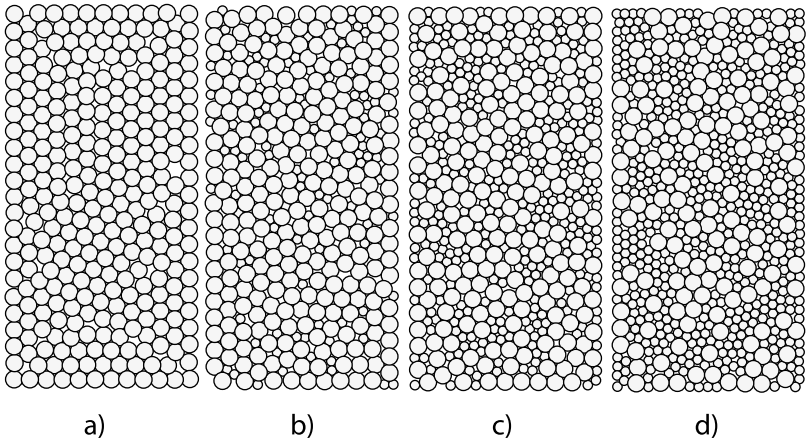

Figure 10. Two-dimensional model of granular aggregates. (a) Uniform model with the same-size particles (180 μm). (b–d) Models with two different particles; see Table 2. The ratios of particle volume are 9:1, 7:3, and 5:5.

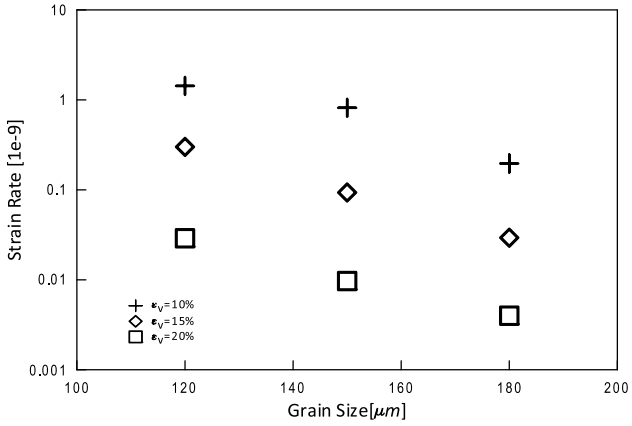

Figure 12. Strain rate of chemical compaction with the certain volume strain in uniform models which have particle sizes of 120, 150, and 180 μm. The smaller the grain size, the greater the volume strain rate at the constant volume strain shown.

increases the compaction rate and results in a faster and greater loss in both porosity and average permeability. Further insight into the role of particle size on the evolution of pressure solution is shown for systems modeled with three different uniform grain sizes of 120, 150, and 180 μm (Figure 12). The models were run with the same loading of 30 MPa and at room temperature of 20°C with the same initial porosity. It is clear from Figure 12 that at the same magnitudes of volume strain, the smaller grain size, the larger strain rate, further certifying that the smaller particles dominate the compaction process.

[26] Temperature also exerts an important effect on the compaction of aggregates [*Yasuhara et al.*, 2003]. When temperature is increased and with all other conditions held constant an increase in temperature both accelerates compaction and increases the ultimate loss of porosity (Figure 13). This shows the evolution of porosity for a moderately heterogeneous aggregate (160–320 μm) where the equilibrium porosity is 14.5% for T = 20°C and reduces to 11.5% at T = 300°C. It is clear that the higher the temperature, the greater the loss in porosity and the faster the rate of dissolution in this granular aggregate. The critical stress that controls the ultimate magnitude of chemical compaction is a function of absolute temperature; the higher the temperature, the lower the critical stress. Equation (6) indicates that the compaction rate correlates negatively against the critical stress in this dissolution-mediated system with the same mechanical loading. Also it is clear from Figure 13 that the rate of porosity loss is larger at higher temperatures.

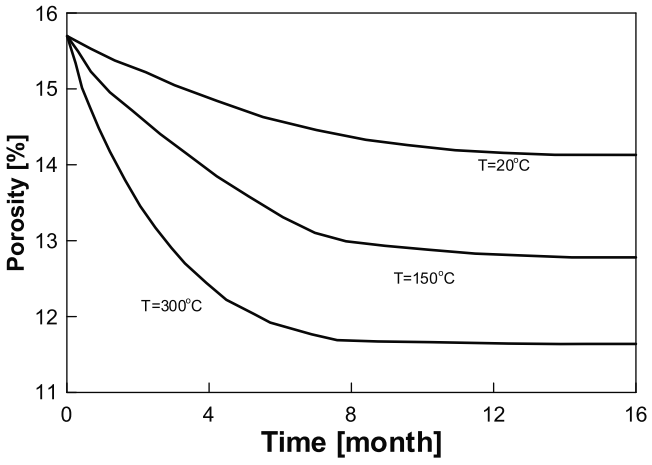

Figure 13. Influence of temperature on porosity evolution for a heterogeneous granular pack with grain sizes in the range of 160 to 480 μm (model 3). Models are under a load of 20 MPa.

[27] Finally, for a Gaussian model representing a real system in long-term compaction, an analysis was executed at different mechanical loading with particle sizes from 160 to 350 μm. Strain in the loading direction and average permeability in the model are compared in Figure 14. Strain and permeability evolve with chemomechanical compaction in the open system; permeability decreases as compactive strain increases. This corresponds to other experimental observation and numerical calculations [*Niemeijer et al.*, 2002; *Yasuhara et al.*, 2003].

4.4. Permeability Numerical Experiment

[28] Permeability evolution is related to porosity evolution with dominant overprinted controls of grain size and pore diameter, their evolution in time and their connectedness. In

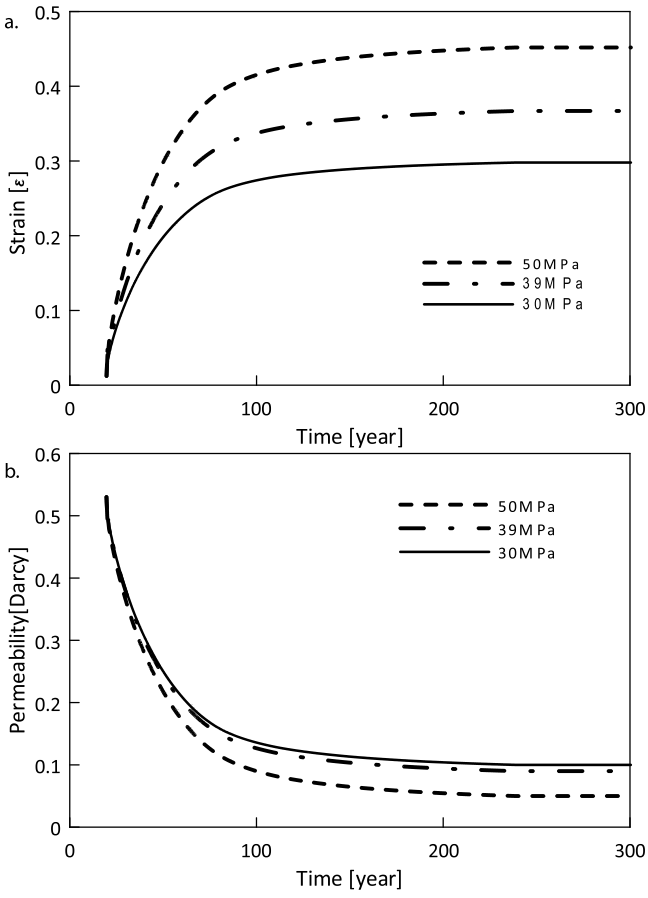

Figure 14. Evolution of the (top) vertical strain and (bottom) permeability in different effective stress at the open system with the model of Gaussian distribution (160–350 μm).

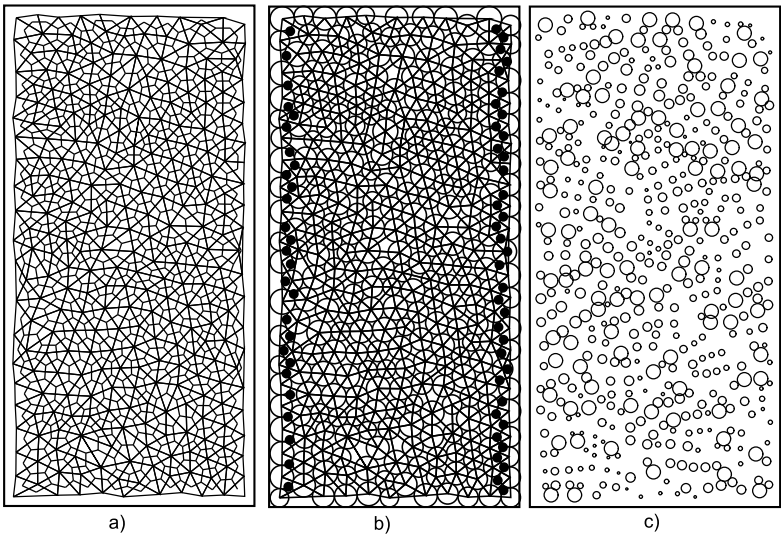

Figure 15. Fluid network and fluid boundary conditions in the model for a numerical experiment of flow. (a) Fluid domain (each triangle element is one fluid domain; thick black line) and flow network (formed by flow path; thin black line connecting the two adjacent fluid domains). (b) Darcy flow model boundary, where (left) pl = 1 MPa and (right) pr = 0 MPa. The solid black dots show the boundary fluid domain with fixed pressures. (c) Local permeability in the model. Large to small circles indicate permeability on the order of 1 darcy to 20 mdarcy.

our model, on the basis of the particle-particle contact shape, local permeability is calculated from equation (28). Figure 15c shows the heterogeneous local permeability of each flow path distributed within the sample. In this, local permeability is only a partial indicator of the global evolution of permeability during chemical compaction and the mathematic mean of local permeability which is called average permeability can be traced in granular model to show the trend of permeability during compaction. And it is this global permeability that is desired because of its importance on fluid, mass, and energy transport. We follow this behavior by conducting a numerical flow-through experiment representing Darcy flow to calculate the global permeability at certain stages during chemical compaction. Figures 15a and 15b are the fluid domain and fluid network for the flow-through experiment. With the relation of the direction of fluid flow through the model and the direction of mechanical loading, we have Darcy test 1 which fluid flow direction is perpendicular to mechanical loading, and Darcy test 2 which fluid flow direction is parallel to mechanical loading. Permeability from these two tests was called perpendicular permeability or series permeability and parallel permeability. The fluid heads were set to 1 and 0 MPa, with the other two side boundaries to no flow. We represent the cumulative flow rate from the system using Darcy's law, as

$$k = -\frac{Q}{A}\frac{L\mu}{\Delta P} \tag{30}$$

where Q is the total fluid flow rate out of the system, A is the macroscopic cross-sectional area, L is the length of the sample, μ is the fluid viscosity and ΔP is the pressure difference across the sample. We examine the evolution of permeability when flow is aligned both parallel and perpendicular to the direction of mechanical loading (compaction) (see Figure 16).

[29] During chemical compaction, the permeability decreases with time (see Figure 16, solid line). The average permeability based on the local permeability is calculated at the same sampling times of the numerical flow-through experiment as

$$k_{av} = \frac{\sum k_{local}}{n_f} \tag{31}$$

where k_{av} is the average permeability, k_{local} is local permeability and n_f is the number of active flow paths. The result

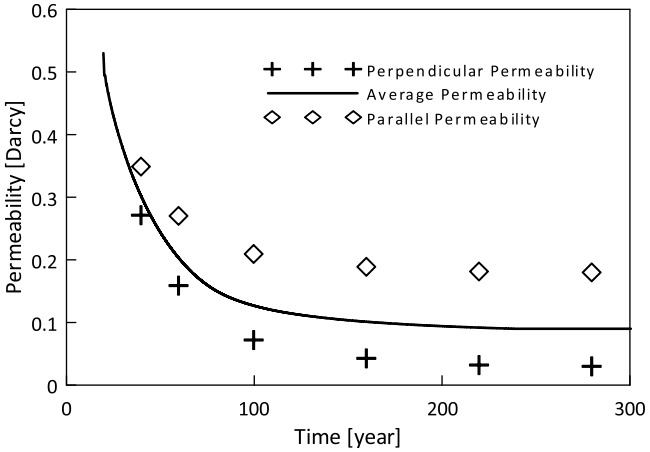

Figure 16. Comparison of the Anthem permeability which is parallel to mechanical loading, average permeability which is mean of the local permeability calculated in the model on the basis of the shape of fluid path in each local contact, and series permeability which is perpendicular to mechanical loading of granular aggregates at the loading of 39 MPa.

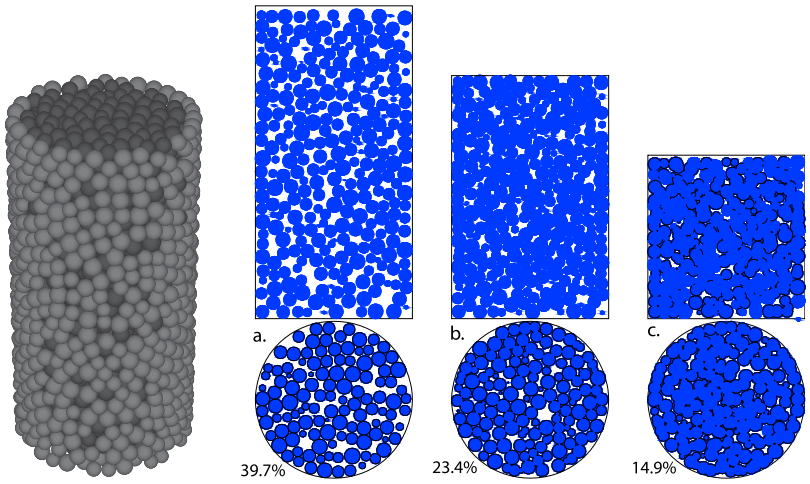

Figure 17. Three-dimensional model with the particles in the range of (180–250 μm); the radius is 2 mm and height is 4 mm. (a–c) Snapshots of particles distribution in the 3-D model during chemomechanical compaction. The porosity of each is marked by the horizontal middle section; they are 39.7%, 23.4%, and 14.9%.

of this calculation is also shown in Figure 15c. The average permeability is always greater than the global permeability during chemical compaction and before peak loading. Before failure, in any fluid flow path which traverses the sample, the narrowest section with the smallest local permeability will control the flow behavior.

[30] This numerical flow-through experiment shows that the average permeability is not the true macroscopic permeability of the heterogeneous granular aggregate. The magnitude of the porosity, the connection of each pore and even hydraulic loading affects the macroscopic permeability which is a tensor. On the basis of this experiment we observe that the permeability measured parallel to the direction of the applied stress is larger than the average permeability which is the mean value of the local permeability. The permeability measured in the direction perpendicular the applied stress (series permeability) is the smallest. With the chemo-mechanical compaction, the particles move laterally which reduces the pore volume and decreases the connection in the horizontal direction with vertical loading. The evolution of average permeability is bounded by the lower permeability perpendicular to the loading and higher permeability parallel to the loading.

4.5. Three-Dimensional Model

[31] The difference in vertical and horizontal permeability also can be rigorously illustrated with the 3-D model shown in Figures 17a–17c, which are the cross-sectional snapshots of the sample during compaction. Figures 17a–17c show the particle assemblage becoming increasingly more dense with compaction where the porosity before loading of ~35% decreases to ~15% at the end of chemical compaction. From these cross-sectional snapshots we also observe that with compaction the particles translate laterally and move closer to fill the pore space and block the fluid flow pathways in the horizontal direction, and pores still connected in the vertical direction.

[32] A comparison of the 2-D and 3-D models for porosity evolution with same loading condition (σ_{eff} = 39 MPa) during compaction is shown in Figure 18. The porosity loss is faster in the same time period in the 3-D model than in the 2-D model for chemomechanical compaction. The increase in the number of translational degrees of freedom in the system is the reason for this difference. The potential modes of compaction are increased in the 3-D model owing to the lack of constrain in the plane direction. As a result the stress intensity decreases in the aggregate as a result of the particulate aggregate becoming more uniform. As a result of this compaction the mechanical strength of the aggregate will increase and will be discussed in later work.

5. Conclusion

[33] A coupled chemical-mechanical model is used to represent the compaction of a granular system. This is achieved

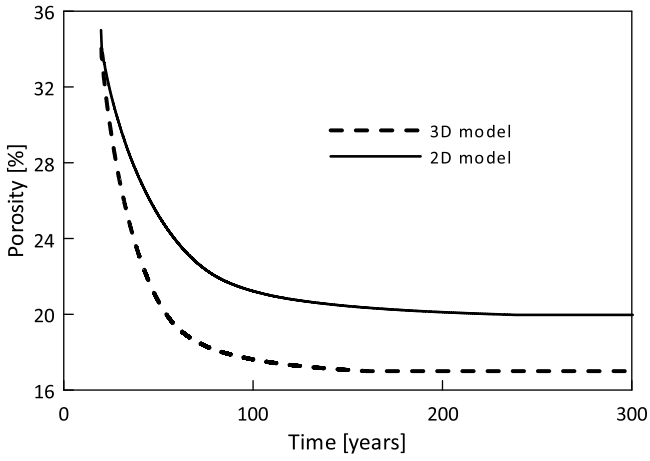

Figure 18. Comparison of the evolution of porosity in 2-D and 3-D granular models that were set the same initial porosity and loading condition. Because of the increase of freedom in lateral direction, the porosity decreased faster and more in the 3-D model compared with the 2-D model.

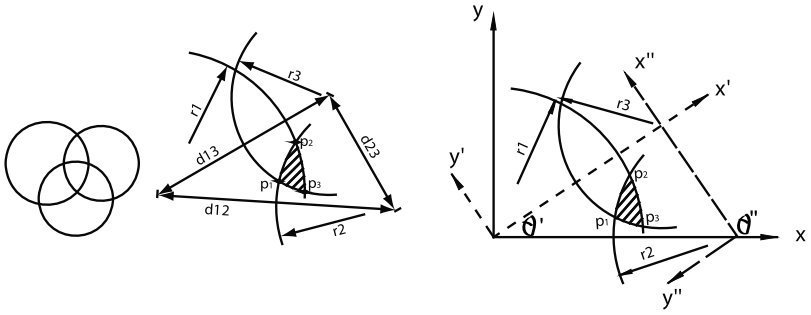

Figure A1. Schematic showing the area (cross-hatched area) of common overlap of three circles, o1, o2, and o3 (here the coordinate of p1, p2, and p3 are (x23, y23), (x12, y12), and (x13, y13)) used to evaluate dissolved mass in the contact between particles.

by developing and implementing a new model to represent the granular mechanisms that represent stress-mediated chemical compaction. This model accommodates a coupled algorithm to represent pressure solution creep accommodated as the three serial processes of dissolution, diffusion and reprecipitation. Bead packs with different particle size gradations were used to explore the role of heterogeneity including those with uniform and Gaussian distributions, each with a common porosity of ~16%, bimodal with particles either 100 or 180 μm. All the porosity and permeability evolution asymptotes showed that the small particles in the system will dominate this dissolution-mediated compaction process. The comparison of uniform model with bimodal with different volume ratio of particles illustrated this rigorously. As the proportion of small particles increases the loss in porosity is also increased. For nonisothermal systems, temperature is shown to have a significant influence on the rate of chemical compaction; higher temperatures result in faster rates of compaction and greater magnitudes of compaction. This results from the Arrhenius dependency of diffusion coefficient and critical stress on temperature. It is verified by the comparison of the porosity rate evolution of this work with that from the experiment result of *Niemeijer et al.* [2002].

[34] Evolution of permeability shows the same trend to that of porosity especially the local permeability which is a partial function of the porosity based on equation (26). But for the macroscopic permeability in heterogeneous aggregates, which is a tensor, it is much more complicated. Some factors such as loading rate and the condition of connection of each adjacent pore domain exert a significant influence on the global permeability. Numerical flow-through experiments show the evolution of average permeability and follow the changing trend of macroscopic permeability. Also the permeability in the direction parallel to the applied stress is greater than the average permeability which in turn is greater than the permeability in the direction perpendicular to the applied stress. The 3-D model illustrates this and in comparison with the 2-D model shows that increased degrees of displacement freedom of particles also increases the compaction rate.

[35] Finally, the coupling due to the effects of feedback of the chemical compaction on the mechanical behavior makes the granular system more uniform, more compact, and ultimately stiffer and stronger which will have additional impacts on the evolution of permeability.

Appendix A: Particle Interpenetration Analysis

[36] In this work, the particle will overlap with the ones that surround it. The situation of three particles overlapping each other (see Figure A1) is common. Here the algorithm of the area of common overlap of three circles is simply given as followed. The input parameters are the three radii, ordered so that $r_1 \geq r_2 \geq r_3$, and the three separations of circle centers d_{12}, d_{13}, d_{23}, as illustrated in Figure A1. The steps required to compute the area of the circular triangle are:

[37] Step 1: Check whether circles 1 and 2 intersect by testing d_{12}. If

$$r_1 - r_2 < d_{12} < r_1 + r_2 \tag{A1}$$

is not satisfied, then there is no circular triangle and the algorithm terminates.

[38] Step 2: Calculate the coordinates of the relevant intersection point of circles 1 and 2 (see Figure A1):

$$x_{12} = \frac{r_1^2 - r_2^2 + d_{12}^2}{2d_{12}},$$

$$y_{12} = \frac{1}{2d_{12}}\sqrt{2d_{12}^2(r_1^2 + r_2^2) - (r_1^2 - r_2^2)^2 - d_{12}^4}. \tag{A2}$$

[39] Step 3: Calculate the values of the sines and cosines of the angles θ' and θ'':

$$\cos\theta' = \frac{d_{12}^2 + d_{13}^2 - d_{23}^2}{2d_{12}d_{13}}, \sin\theta' = \sqrt{1 - \cos^2\theta'}$$

$$\cos\theta'' = \frac{d_{12}^2 + d_{23}^2 - d_{13}^2}{2d_{12}d_{23}}, \sin\theta'' = \sqrt{1 - \cos^2\theta''}. \tag{A3}$$

[40] Step 4: Check that circle 3 is placed so as to form a circular triangle. The conditions

$$(x_{12} - d_{13}\cos\theta')^2 + (y_{12} - d_{13}\sin\theta')^2 < r_3^2$$

$$(x_{12} - d_{13}\cos\theta')^2 + (y_{12} + d_{13}\sin\theta')^2 > r_3^2 \tag{A4}$$

must both be satisfied. Otherwise, there is no circular triangle and the algorithm terminates.

[41] Step 5: Calculate the values of the coordinates of the relevant intersection points involving circle 3:

$$x_{13}^{'} = \frac{r_1^2 - r_3^2 + d_{13}^2}{2d_{13}},$$
$$y_{13}^{'} = \frac{-1}{2d_{12}}\sqrt{2d_{13}(r_1^2 + r_3^2) - (r_1^2 - r_3^2)^2 - d_{13}^4} \quad \text{(A5)}$$

$$x_{13} = x_{13}^{'}\cos\theta^{'} - y_{13}^{'}\sin\theta^{'},\ y_{13} = x_{13}^{'}\sin\theta^{'} + y_{13}^{'}\cos\theta^{'}$$
$$x_{23}^{''} = \frac{r_1^2 - r_3^2 + d_{23}^2}{2d_{23}}, y_{23}^{''} = \frac{1}{2d_{23}}\sqrt{2d_{23}(r_2^2 + r_3^2) - (r_2^2 - r_3^2)^2 - d_{23}^4}. \quad \text{(A6)}$$

[42] Step 6: Use the coordinates of the intersection points to calculate the chord lengths c_1, c_2, c_3:

$$c_k^2 = (x_{ik} - x_{jk})^2 + (y_{ik} - y_{jk})^2. \quad \text{(A7)}$$

[43] Step 7: Check whether more than half of circle 3 is included in the circular triangle, so as to choose the correct expression for the area. That is, determine whether

$$d_{13}\sin\theta^{'} < y_{13} + \frac{y_{23} - y_{13}}{x_{13} - x_{13}}(d_{13}\cos\theta^{'} - x_{13}) \quad \text{(A8)}$$

is true or false. The area is given by

$$A = \frac{1}{4}\sqrt{(c_1 + c_2 + c_3)(-c_1 + c_2 + c_3)(c_1 - c_2 + c_3)(c_1 + c_2 - c_3)} + \sum_{k=1}^{3}\left(r_k^2 \arcsin\frac{c_k}{2r_k}\right) - \sum_{k=1}^{2}\frac{c_k}{4}\sqrt{4r_k^2 - c_k^2} + \begin{cases} \frac{c_3}{4}\sqrt{4r_3^2 - c_3^2} \\ \frac{-c_3}{4}\sqrt{4r_3^2 - c_3^2} \end{cases}. \quad \text{(A9)}$$

[44] **Acknowledgments.** This work is the result of partial support from the Department of Energy's Office of Energy Efficiency and Renewable Energy and Geothermal Technology Program under contract EE-10EE0002761. This support is gratefully acknowledged.

References

Andre, L., P. Audigane, M. Azaroual, and A. Menjoz (2007), Numerical modeling of fluid-rock chemical interactions at the supercritical CO_2-liquid interface during CO_2 injection into a carbonate reservoir, the Dogger aquifer (Paris Basin, France), *Energy Convers. Manage.*, *48*, 1782–1797, doi:10.1016/j.enconman.2007.01.006.

Bear, J. (1972), *Dynamics of Fluids in Porous Media*, Dover, Mineola, N. Y.

Bekri, S., J. F. Thovert, and P. M. Adler (1995), Dissolution of porous-media, *Chem. Eng. Sci.*, *50*, 2765–2791, doi:10.1016/0009-2509(95)00121-K.

Bekri, S., J. F. Thovert, and P. M. Adler (1997), Dissolution and deposition in fractures, *Eng. Geol. Amsterdam*, *48*, 283–308, doi:10.1016/S0013-7952(97)00044-6.

Bemer, E., and J. M. Lombard (2010), From injectivity to integrity studies of CO_2 geological storage chemical alteration effects on carbonates petrophysical and geomechanical properties, *Oil Gas Sci. Technol.*, *65*, 445–459, doi:10.2516/ogst/2009028.

Chester, F. M., J. S. Chester, A. K. Kronenberg, and A. Hajash (2007), Subcritical creep compaction of quartz sand at diagenetic conditions: Effects of water and grain size, *J. Geophys. Res.*, *112*, B06203, doi:10.1029/2006JB004317.

Cussler, E. L. (1982), Dissolution and re-precipitation in porous solids, *AIChE J.*, *28*, 500–508, doi:10.1002/aic.690280320.

Dewers, T., and A. Hajash (1995), Rate laws for water-assisted compaction and stress-induced water-rock interaction in sandstones, *J. Geophys. Res.*, *100*, 13,093–13,112, doi:10.1029/95JB00912.

Elias, B. P., and A. Hajash (1992), Changes in quartz solubility and porosity due to effective stress—An experimental investigation of pressure solution, *Geology*, *20*, 451–454, doi:10.1130/0091-7613(1992)020<0451:CIQSAP>2.3.CO;2.

Goodman, R. E. (1980), *Introduction to Rock Mechanics*, John Wiley, New York.

Gundersen, E., F. Renard, D. K. Dysthe, K. Bjørlykke, and B. Jamtveit (2002), Coupling between pressure solution creep and diffusive mass transport in porous rocks, *J. Geophys. Res.*, *107*(B11), 2317, doi:10.1029/2001JB000287.

He, W. W., A. Hajash, and D. Sparks (2003), Creep compaction of quartz aggregates: Effects of pore-fluid flow, A combined experimental and theoretical study, *Am. J. Sci.*, *303*, 73–93, doi:10.2475/ajs.303.2.73.

Heidug, W. K. (1995), Intergranular solid-fluid phase transformations under stress: The effect of surface forces, *J. Geophys. Res.*, *100*, 5931–5940, doi:10.1029/94JB03100.

Itasca Consulting Group, Inc. (2007), *PFC2D (Particle Flow Code in 2 Dimensions)*, Minneapolis, Minn.

Lehner, F. K. (1995), A model for intergranular pressure solution in open systems, *Tectonophysics*, *245*, 153–170, doi:10.1016/0040-1951(94)00232-X.

Niemeijer, A., C. J. Spiers, and B. Bos (2002), Compaction creep of quartz sand at 400–600 degrees C: Experimental evidence for dissolution-controlled pressure solution, *Earth Planet. Sci. Lett.*, *195*, 261–275, doi:10.1016/S0012-821X(01)00593-3.

Niemeijer, A., C. Marone, and D. Elsworth (2010), Frictional strength and strain weakening in simulated fault gouge: Competition between geometrical weakening and chemical strengthening, *J. Geophys. Res.*, *115*, B10207, doi:10.1029/2009JB000838.

Paterson, M. S. (1973), Nonhydrostatic thermodynamics and its geologic applications, *Rev. Geophys.*, *11*, 355–389, doi:10.1029/RG011i002p00355.

Polak, A., D. Elsworth, J. Liu, and A. S. Grader (2004), Spontaneous switching of permeability changes in a limestone fracture with net dissolution, *Water Resour. Res.*, *40*, W03502, doi:10.1029/2003WR002717.

Raj, R. (1982), Creep in polycrystalline aggregates by matter transport through a liquid phase, *J. Geophys. Res.*, *87*, 4731–4739, doi:10.1029/JB087iB06p04731.

Renard, F., P. Ortoleva, and J. P. Gratier (1997), Pressure solution in sandstones: Influence of clays and dependence on temperature and stress, *Tectonophysics*, *280*, 257–266, doi:10.1016/S0040-1951(97)00039-5.

Revil, A. (1999), Pervasive pressure-solution transfer: A poro-visco-plastic model, *Geophys. Res. Lett.*, *26*, 255–258, doi:10.1029/1998GL900268.

Revil, A. (2001), Pervasive pressure solution transfer in a quartz sand, *J. Geophys. Res.*, *106*, 8665–8686, doi:10.1029/2000JB900465.

Rutter, E. H. (1976), Kinetics of rock deformation by pressure solution, *Philos. Trans. R. Soc. Ser. A*, *283*, 203–219, doi:10.1098/rsta.1976.0079.

Scheidegger, A. E. (1960), Growth of instabilities on displacement fronts in porous media, *Phys. Fluids*, *3*, 94–104, doi:10.1063/1.1706009.

Schutjens, P. M. T. M., and C. J. Spiers (1999), Intergranular pressure solution in NaCl: Grain-to-grain contact experiments under the optical microscope, *Oil Gas Sci. Technol.*, *54*, 729–750.

Shimizu, I. (1995), Kinetics of pressure solution creep in quartz—Theoretical considerations, *Tectonophysics*, *245*, 121–134, doi:10.1016/0040-1951(94)00230-7.

Singh, B. (1973a), Continuum characterization of jointed rock masses. 1. Constitutive equations, *Int. J. Rock Mech. Min. Sci.*, *10*, 311–335, doi:10.1016/0148-9062(73)90041-7.

Singh, B. (1973b), Continuum characterization of jointed rock masses. 2. Significance of low shear modulus, *Int. J. Rock Mech. Min. Sci.*, *10*, 337–349, doi:10.1016/0148-9062(73)90042-9.

Sleep, N. H., E. Richardson, and C. Marone (2000), Physics of friction and strain rate localization in synthetic fault gouge, *J. Geophys. Res.*, *105*, 25,875–25,890, doi:10.1029/2000JB900288.

Stephanson, O. (1985), Fundamentals of rock joints, paper presented at International Symposium on Fundamentals of Rock Joints, Int. Soc. Rock Mech., Björkliden, Sweden.

Tada, R., and R. Siever (1989), Pressure solution during diagenesis, *Annu. Rev. Earth Planet. Sci.*, *17*, 89–118, doi:10.1146/annurev.ea.17.050189.000513.

Taron, J., and D. Elsworth (2010), Coupled mechanical and chemical processes in engineered geothermal reservoirs with dynamic permeability, *Int. J. Rock Mech. Min. Sci.*, *47*, 1339–1348, doi:10.1016/j.ijrmms.2010.08.021.

Van Bramer, S. E. (2007), A brief introduction to the Gaussian distribution, sample statistics, and the Student's *t* statistic, *J. Chem. Educ.*, *84*(7), 1231, doi:10.1021/ed084p1231.2.

Yasuhara, H., D. Elsworth, and A. Polak (2003), A mechanistic model for compaction of granular aggregates moderated by pressure solution, *J. Geophys. Res.*, *108*(B11), 2530, doi:10.1029/2003JB002536.

Yasuhara, H., D. Elsworth, and A. Polak (2004), Evolution of permeability in a natural fracture: Significant role of pressure solution, *J. Geophys. Res.*, *109*, B03204, doi:10.1029/2003JB002663.

Yasuhara, H., C. Marone, and D. Elsworth (2005), Fault zone restrengthening and frictional healing: The role of pressure solution, *J. Geophys. Res.*, *110*, B06310, doi:10.1029/2004JB003327.

D. Elsworth and B. Zheng, Energy and Mineral Engineering and Energy Institute, Pennsylvania State University, University Park, PA 16802, USA. (bshzheng@gmail.com)